

Frequency-modulated continuous-wave multiplexed gas sensing based on optical frequency comb calibration

Linhua Jia(贾琳华), Xinghua Qu(曲兴华), and Fumin Zhang (张福民)

Citation: Chin. Phys. B, 2024, 33 (**9**): 094201. DOI: 10.1088/1674-1056/ad5980
Journal homepage: http://cpb.iphy.ac.cn; http://iopscience.iop.org/cpb

What follows is a list of articles you may be interested in

Numerical study of converting beat-note signals of dual-frequency lasers to optical frequency combs by optical injection locking of semiconductor lasers

Chenhao Liu(刘晨浩), Haoshu Jin(靳昊澍), Hui Liu(刘辉), and Jintao Bai(白晋涛)
Chin. Phys. B, 2022, 31 (**8**): 084205. DOI: 10.1088/1674-1056/ac649a

Precise determination of characteristic laser frequencies by an Er-doped fiber optical frequency comb

Shiying Cao(曹士英), Yi Han(韩羿), Yongjin Ding(丁永今), Baike Lin(林百科), and Zhanjun Fang(方占军)
Chin. Phys. B, 2022, 31 (**7**): 074207. DOI: 10.1088/1674-1056/ac5608

Generation of stable and tunable optical frequency linked to a radio frequency by use of a high finesse cavity and its application in absorption spectroscopy

Yueting Zhou(周月婷), Gang Zhao(赵刚), Jianxin Liu(刘建鑫), Xiaojuan Yan(闫晓娟), Zhixin Li(李志新), Weiguang Ma(马维光), and Suotang Jia(贾锁堂)
Chin. Phys. B, 2022, 31 (**6**): 064206. DOI: 10.1088/1674-1056/ac4905

All polarization-maintaining Er:fiber-based optical frequency comb for frequency comparison of optical clocks

Pan Zhang(张攀), Yan-Yan Zhang(张颜艳), Ming-Kun Li(李铭坤), Bing-Jie Rao(饶冰洁), Lu-Lu Yan(闫露露), Fa-Xi Chen(陈法喜), Xiao-Fei Zhang(张晓斐), Qun-Feng Chen(陈群峰), Hai-Feng Jiang(姜海峰)[‡], and Shou-Gang Zhang(张首刚)
Chin. Phys. B, 2022, 31 (**5**): 054210. DOI: 10.1088/1674-1056/ac40f6

Mid-infrared supercontinuum and optical frequency comb generations in a multimode tellurite photonic crystal fiber

Xu Han(韩旭), Ying Han(韩颖), Chao Mei(梅超), Jing-Zhao Guan(管景昭), Yan Wang(王彦), Lin Gong(龚琳), Jin-Hui Yuan(苑金辉), and Chong-Xiu Yu(余重秀)
Chin. Phys. B, 2021, 30 (**9**): 094207. DOI: 10.1088/1674-1056/abf10f

---

INSTRUMENTATION AND MEASUREMENT

Frequency-modulated continuous-wave multiplexed gas sensing based on optical frequency comb calibration

Linhua Jia(贾琳华), Xinghua Qu(曲兴华), and Fumin Zhang (张福民)[†]

State Key Laboratory of Precision Measurement Technology and Instruments, Tianjin University, Tianjin 300072, *China*

(Received 17 May 2024; revised manuscript received 6 June 2024; accepted manuscript online 19 June 2024)

Laser absorption spectroscopy has proven to be an effective approach for gas sensing, which plays an important role in the fields of military, industry, medicine and basic research. This paper presents a multiplexed gas sensing system based on optical frequency comb (OFC) calibrated frequency-modulated continuous-wave (FMCW) tuning nonlinearity. The system can be used for multi-parameter synchronous measurement of gas absorption spectrum and multiplexed optical path. Multi-channel parallel detection is realized by combining wavelength division multiplexing (WDM) and frequency division multiplexing (FDM) techniques. By introducing nonlinear optical crystals, broadband spectrum detection is simultaneously achieved over a bandwidth of hundreds of nanometers. An OFC with ultra-high frequency stability is used as the frequency calibration source, which guarantees the measurement accuracy. The test samples involve $H^{13}C^{14}N$, C_2H_2 and Rb vapor cells of varying densities and 5 parallel measurement experiments are designed. The results show that the measurement accuracies of spectral absorption line and the optical path are 150 MHz and 20 μm, respectively. The scheme offers the advantages of multiplexed, multi-parameter, wide spectrum and high resolution detection, which can realize the identification of multi-gas components and the high-precision inversion of absorption lines under different environments. The proposed sensor demonstrates great potential in the field of high-resolution absorption spectrum measurement for gas sensing applications.

Keywords: frequency-modulated continuous-wave (FMCW) technology, optical frequency comb, multiplexing, absorption spectroscopy

PACS: 42.15.Eq, 06.20.–f, 42.62.Fi, 42.62.–b **DOI:** 10.1088/1674-1056/ad5980

1. Introduction

Laser absorption spectroscopy has been utilized for trace gas detection,[1,2] industrial pollution monitoring,[3] military target detection[4] and combustion field diagnosis,[5] due to its ability to measure the electromagnetic field related to the internal energy distribution and energy level transition of the measured object. Since it offers the advantages of non-contact, high sensitivity, high resolution, and *in-situ* online detection, it has become one of the most widely used spectral detection methods.[6] In the traditional detection scheme, the optical path measurement is pre-determined and independent of the absorption spectrum. However, in complex or unknown environments such as engine combustion chamber measurement,[7] industrial pollution emission[8] and gas pipeline gas monitoring,[9] it is challenging to accurately carry out gas detection using pre-calibrated optical paths. In addition, the detection scheme of single target point or single path is not suitable for large-scale or complex scenes. At present, techniques such as tunable diode laser absorption spectroscopy (TDLAS) are based on tunable semiconductor lasers with narrow laser line width and wavelength varying with injection current.[10,11] This method can achieve the concentration accuracy of ppm level, and realize the distinction of aliasing absorption lines in complex gas fields.[12] However, this scheme can only obtain a narrow band scan of one absorption spectral line. Additionally, it does not have the ability to capture range-resolved information and can only perform line-of-sight measurement. Dual-comb spectroscopy (DCS) overcomes these drawbacks by using two femtosecond optical frequency combs with slightly different repetition rates for optical heterodyne detection.[13,14] This strategy enables high-precision measurement of absorption spectra with a bandwidth of tens to hundreds of nanometers without the need for mechanical scanning or dispersive elements. However, it is challenging to achieve multiplexed detection with the DCS system in a single photodetector unit configuration. It requires a complex frequency stabilization phase locking system to maintain frequency stability and high coherence between dual comb light sources, which greatly increases the complexity and cost of the system. Therefore, achieving a high-precision laser absorption spectrum measurement system that can realize ultra-high resolution gas component detection, high-precision optical path measurement and multiplexing can be extremely advantageous.

The frequency-modulated continuous-wave (FMCW) technology can combine the advantages of high-precision detection of absorption spectroscopy and active detection ability of laser radar.[15–17] This merger has been gathering attention

[†]Corresponding author. E-mail: zhangfumin@tju.edu.cn

© 2024 Chinese Physical Society and IOP Publishing Ltd

in the field of laser coherence detection as it can meet the requirements of multiplex detection of absorption spectral information and multiplexed optical path. The basic principle of laser absorption spectrum detection based on FMCW involves the use of a linearly modulated continuous-wave (CW) laser, where the absorption spectral lines of different components on the integral path are retrieved by detecting the coherent signal and local oscillator of the echo. The light source uses a long light pulse with continuous frequency tuning, which enables the bandwidth to reach tens of nanometers. The combination of wavelength division multiplexing (WDM) and frequency division multiplexing (FDM) schemes can realize multiplexed measurement using a single light source and a single detection unit, where different gas components can be resolved under different paths. Due to rapid development of nonlinear optics and optoelectronics technology, FMCW can be combined with specific crystals to achieve efficient laser frequency conversion and spectrum expansion, which increases the range of detected gases and expands the application scope.[18,19] Compared with the traditional direct absorption method, the FMCW method sinusoidally modulates the absorption information, which not only facilitates a high signal-to-noise ratio (SNR) spectral measurement, but also achieves optical path resolution with micron level accuracy.[20,21]

In addition, the use of an optical frequency comb (OFC) as the frequency calibration source of the FMCW absorption spectrum measurement system overcomes the tuning nonlinearity of the light source. An OFC can be considered as a light source with a broadband spectrum that is composed of a series of discrete, fixed and equispaced frequency components, where the phase relationship between the frequency components is stable.[22–24] Such a source can provide a wide spectrum laser that is traceable to the microwave frequency reference for the calibration of the laser frequency to be measured.[25,26] Using OFC as a reference for FMCW frequency calibration achieves wide spectral range calibration ($\sim$ 100 nm) and high-frequency stability (10^{-12} @1 s) while avoiding the dispersion problem caused by the auxiliary path fiber in the traditional resampling scheme, and expands the measurable optical range.

In this paper, an FMCW absorption spectrum detection system is designed based on the OFC nonlinear calibration. The system can realize the simultaneous high precision measurement of absorption spectrum and multiplexed optical path. Compared with the traditional device, multiplexed detection in a single detection unit is realized based on the principle of WDM and FDM by introducing a coarse wavelength division multiplexing (CWDM) device. Combined with periodically polarized lithium niobate (PPLN) crystal, the device can achieve the wide spectrum detection across several hundreds of nanometers, and can simultaneously detect the molecular and atomic absorption spectra. As a frequency calibration source, OFC has the characteristics of large bandwidth, narrow line width, high frequency accuracy and excellent timing stability, which guarantees a high degree of measurement accuracy. The proposed scheme makes full use of the interference information of the measurement path signal for the calculations. Herein, the phase information is used to calibrate tuning nonlinearity; the frequency information is used to calculate the optical path; and the amplitude information is used to analyze the absorption spectrum. The device described in this paper can realize pm-level absorption line detection and μm-level optical path measurement. Overall, the system has the advantages of multi-parameter, wide spectrum, high precision, multi-gas component and multi-channel synchronous online measurement, and exhibits high resolution and high selectivity for the characteristic spectrum detection of the target gas. The scheme demonstrates a new method for gas absorption spectrum analysis, which overcomes existing technical problems encountered in current systems.

2. Measurement principle

2.1. FMCW multi-parameter measurement based on OFC nonlinear calibration

The Beer–Lambert law is the cornerstone of laser absorption spectrum measurement.[27] When the laser beam passes through a gaseous medium, the light intensity will attenuate due to the absorption of the gas. The formula for calculating absorbance A can be expressed as

$$A = \ln\left(\frac{1}{T}\right) = KLC, \tag{1}$$

where T is the transmittance, and K is the absorption coefficient that is related to parameters such as temperature, pressure, type of gas and incident laser frequency. L is the absorption path and C is the gas concentration to be measured. Therefore, the absorption spectrum information of the gas to be measured can be obtained by using a frequency-modulated (FM) light source, tuning the incident laser frequency and detecting the transmitted light intensity. By accurately inverting and fitting the absorption spectral line, the gas type can be identified and its concentration can be determined along with temperature, pressure and other parameters in the measured integral path.

Figure 1(a) shows the optical path diagram of FMCW absorption spectrum measurement. FMCW laser emits a triangular-wave frequency-modulated laser whose frequency changes in a periodic triangle; it increases and then periodically decreases. Only the previous half cycle is used as an example here. After splitting the beam, the outgoing laser enters the Mach–Zehnder interferometer (MZI) measurement path and the tuned nonlinear calibration path based on OFC.

In the measurement path, the FM laser divides the beam again. One beam returns to the original path after passing through the measurement path and combines the beam with the other local oscillator light through the coupler to introduce an optical path difference of $2L$. In the calibration path, the FM laser interferes with OFC. The two-channel beat frequency signal is detected by the photodetectors. The signal detected at the measuring channel can be expressed as

$$I(t,\tau) = V \cdot \sqrt{i_0 i} \cdot \cos\left[2\pi \cdot \int_t^{t+\tau} f_{\mathrm{FM}}(t)\,\mathrm{d}t\right], \tag{2}$$

where V is a constant, i_0 is the local oscillator light intensity of the measuring path, and i is the light intensity of the path to be measured. f_{FM} is the frequency of the FMCW light source that changes over time. τ is the delay introduced by the optical path in the measuring path, given by $\tau = 2L/c$ with the optical path L to be measured. f_0 is the initial frequency of the FM laser, α is the modulation rate and c is the speed of light in a vacuum. In an ideal scenario, $f_{\mathrm{FM}}(t) = f_0 + \alpha t$. The interference signal of the measurement path is a sinusoidal signal with a fixed frequency, given by $f_{\mathrm{M}} = \alpha\tau$.

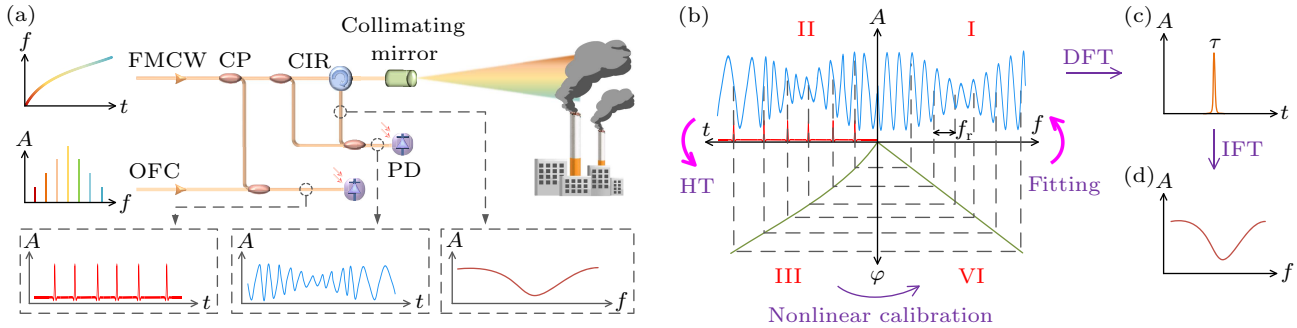


Fig. 1. Schematic diagram of FMCW measurement. (a) Schematic diagram of optical path. CP, coupler. CIR, circulator. PD, photodetector. (b) Schematic of nonlinear calibration. (c) The reflection peak in the pseudo time domain based on discrete Fourier transform (DFT). (d) Absorption lines based on inverse Fourier transform (IFT).

However, the actual laser output deviates from an ideal linear modulation signal due to nonlinear effects in the frequency modulation, which needs to be corrected. Suppose that the phase of the measuring signal is φ_{M}. If higher order Taylor terms are ignored, the relationship between φ_{M} and f_{FM} is a primary function with a coefficient $k = 2\pi\tau$.[28] Therefore, in the case of instantaneous φ_{M} and f_{FM} measurement, the least square method is used to fit the first function of f_{FM}–φ_{M} in order to solve for k. φ_{M} can be solved directly by Hilbert transform (HT) and f_{FM} can be calibrated by OFC.

For linear FM lasers, f_{FM} is continuously tuned between comb modes with equal frequency distribution. The beat interference signals of the two can be detected by the photodetector, where the frequency f_{A} of the interference signals varies between 0 and $f_{\mathrm{r}}/2$. The calibration point of equal frequency interval at $f_{\mathrm{A}} = 0$ can be extracted by filtering, self-convolution and peak-seeking.

The schematic diagram of the principle of nonlinear calibration is shown in Fig. 1(b), where the second quadrant represents the original time domain signal of the double optical path. The third quadrant contains the calibration point of equal frequency interval and corresponding φ_{M}, which has obvious tuning nonlinearity.

The fourth quadrant contains the f_{FM}–φ_{M} line obtained by fitting. After nonlinear calibration, φ_{M} is theoretically a linear function. Therefore, the single frequency sinusoidal signal shown in the first quadrant can be obtained by re-interpolating the measurement path signal in Fig. 2(a). Since f_{FM} changes linearly with time after correction, the original time domain signal is transformed into the pseudo-frequency domain here, and the original time variable t is represented by the optical frequency variable f in the first quadrant of Fig. 1(b). Equation (2) can be converted to

$$I(f,\tau) = V \cdot \sqrt{i_0 i} \cdot \cos(2\pi\tau f). \tag{3}$$

On this basis, DFT calculation is carried out to obtain the pseudo-time domain signal shown in Fig. 1(c), whose peak position corresponds to the delay τ to be measured. The M data points are intercepted symmetrically on the left and right sides of the reflection peak, and the window function filtering is performed. IFT is applied to the filtered data to restore the timing information, and the absorption spectral curve in the optical frequency domain is obtained,[29] as shown in Fig. 1(d). The resolution of DFT is directly related to the sweep frequency range B of FMCW and can be expressed as $\Delta\tau = 1/B$. Therefore, the optical path to be measured can be expressed as $L = c\tau/2$, and the optical path measurement resolution is $\Delta L = c/(2B)$. The resolution of IFT also depends on the number of points M involved in the calculation, which can be expressed as $\Delta f = B/M$, that is, the spectral measurement resolution.

2.2. Multiplexed detection and frequency doubling detection

Although multiplexing is more complex compared to single channel measurements, it can greatly improve the mea-

surement efficiency and facilitate the construction of monitoring networks. By FDM[30] of measurement signals, or WDM[31,32] of linearly tuned light sources, multi-target point differentiation and multiplex detection can be achieved. The realization of FDM can be achieved using couplers and other spectral devices at the detection end to split the detection light into multiple beams, as shown in Fig. 2(a). According to Eq. (2), the measurement signal of the N-channel parallel measurement system can be expressed as

$$I_N(t,\tau) = V\sum_{k=1}^{N}\left\{\sqrt{i_0 i_k}\cos\left[2\pi\int_t^{t+\tau_k} f_{\mathrm{FM}}(t)\,\mathrm{d}t\right]\right\} + V\sum_{x=1}^{N-1}\sum_{y=x+1}^{N}\left\{\sqrt{i_x i_y}\cos\left[2\pi\int_{\tau_x}^{\tau_y} f_{\mathrm{FM}}(t)\,\mathrm{d}t\right]\right\}, \quad (4)$$

where i_k $(k = 1,2,\ldots,N)$ is the return light intensity of the k-th path in the measurement path, and τ_k is the delay introduced by the k-th path. The measurement interference signal is a superposition of multiple sinusoidal signals. Ideally, the frequency component of the k-channel interference signal is $f_k = \alpha\tau_k$. Therefore, different targets can be directly distinguished due to differences in their distances. However, this measurement method can introduce harmonic crosstalk, which will decrease the SNR of the signal as the number of channels is increased. This is where the combination of WDM technology can be beneficial, whose principle is shown in the schematic in Fig. 2(b). The separation of optical signals of different frequencies can be realized by introducing devices such as CWDM or gratings.

In conjunction with multiplexing, optical parametric conversion or harmonic generation of nonlinear crystals can be utilized for cross-band absorption spectrum detection. Using this strategy, the system can be utilized for measuring many kinds of molecular and atomic gases, thereby expanding its capabilities beyond single objects. Here, the laser external cavity resonant frequency multiplier of PPLN crystal is taken as an example. As shown in Fig. 2(c), the frequency doubling process of a beam of fundamental frequency ω light can be divided into two steps: firstly, a polarized wave with frequency 2ω is generated. The phase velocity v_ω of the polarized wave in the center of the frequency doubling crystal depends on the refractive index n_ω of the fundamental frequency, with the wavelength $\lambda_1 = c/(2v_\omega n_\omega)$. Secondly, the energy is converted from the polarized wave to the frequency 2ω electromagnetic wave. The phase velocity $v_{2\omega}$ of the electromagnetic wave is determined by the frequency-doubling optical refractive index $n_{2\omega}$, with the wavelength being $\lambda_2 = c/(2v_{2\omega}n_{2\omega})$. In order to achieve effective energy conversion between the two, it is necessary to ensure that the frequency-doubled light and the polarized wave are in phase. PPLN crystal is a highly efficient non-linear crystal with wavelength conversion, which has a wide transmission range, covering the near and mid infrared region. Efficient phase matching and laser frequency doubling can be realized by proper temperature regulation.

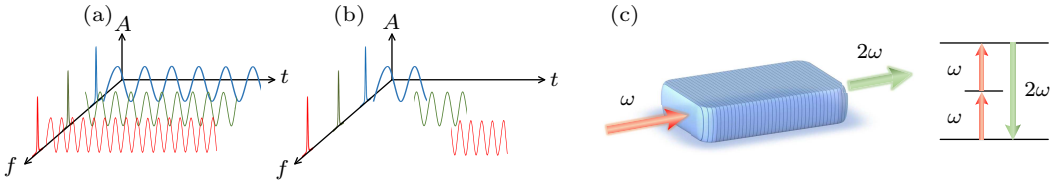


Fig. 2. Schematic diagrams of (a) FDM, (b) WDM, and (c) PPLN frequency doubling crystal.

3. Measurement system

Figure 3 shows a 5-channel parallel measurement device, which is composed of FMCW and OFC light source, measurement optical path and signal acquisition equipment. The experimental system is built on the optical test platform within an ultra-clean laboratory. The optical path includes the dual MZI measurement path, the frequency marking path based on $H^{13}C^{14}N$ (HCN) cell, and the calibration path based on OFC. Different densities of HCN, $^{12}C_2H_2(C_2H_2)$ and Rb cells along with different delays are introduced into the measuring optical path to verify the multiplexing and wide spectrum measurement capability of the system. A tunable laser (Keysight 8164B) is programmed to scan the frequency range of 1525 nm–1575 nm at the rate of 100 nm/s, which includes several absorption peaks of HCN and C_2H_2 cells to be measured. A home-made mode-locked fiber OFC, whose f_r is strictly locked to a rubidium atomic clock,[25,33] serves as a calibration source for tuning nonlinearity and can fully cover the FMCW sweep range with a repetition frequency of 200.15 MHz and a frequency stability better than 2.4×10^{-12} at 1 s. It should be noted that the role of the frequency marking path is used to collect the complete absorption peak signal of R26–R0 and P1–P27 of HCN (25 torr, 5.5 cm), and the specific wavelength value of its peak point is provided by National Institute of Standards and Technology (NIST).[34] The corresponding values of the entire dataset at different sampling points can be obtained using Savitzky–Golay (SG) filtering and Gaussian fitting, and the calibration of the tunable laser wavelength can be realized.[35,36] The interference light signal is detected by four balance detectors (Thorlabs PDB), and the detection bandwidth is limited to 45 MHz. The data is captured and recorded by an oscilloscope (Tektronix MSO64).

In the dual MZI measurement optical path, a four-channel parallel detection is carried out, denoted by CHa–CHd in Fig. 3. CWDM is used to realize the multi-channel detection of WDM. The central wavelengths of the three outgoing terminals are 1570 nm, 1550 nm and 1530 nm, and the passband bandwidth of −3 dB is 10 nm. In order to verify the optical path measurement accuracy of the system, CHa introduces a spatial ranging optical path. The reflection corner cone prism is placed on the horizontal guide rail serving as a target point. The reflection corner cone prism has an isosceles right angle prism structure, which changes the propagation direction of the reflected beam by 180° and returns it to the original path. Another corner cone is placed on the back of the target corner cone, which is used to calibrate the displacement with the incremental laser interferometer (Renishaw XL-80) with nanometer precision. The laser beam of the interferometer is collinear with the spatial light beam of the ranging system. When the target moves, the ranging system and the interferometer will theoretically detect the same displacement value, and comply with the Abbe principle of length measurement, thus eliminating single error interference. CHb and CHc adopt the FDM detection mode comprising of different densities of HCN (25 torr, 16.5 cm and 100 torr, 16.5 cm) gas cells to ascertain the high-precision spectral inversion ability of the system. CHd incorporates HCN (25 torr, 16.5 cm) and C_2H_2 (50 torr, 5.5 cm) cells for determining the resolution ability of the system for multi-component gas mixtures. The other MZI uses the Rb (72.15% ^{85}Rb and 27.85% ^{87}Rb mixed) atomic cell, which is denoted as CHe in Fig. 3. The central wavelength of the filter is set to 1560 nm, whereas the passband bandwidth is set to 5 nm. After the tunable laser passes through the MgO: PPLN crystal, the frequency can be doubled directly to obtain a tunable laser in the 780 nm band. The PPLN chip is integrated and packaged with a fiber-coupled interface, and is controlled by a proportional-integral-derivative (PID) temperature controller with an accuracy of 0.01 °C. Both MZI optical paths of different optical frequency bands can share the same calibration optical path signal to realize tuning nonlinear calibration.

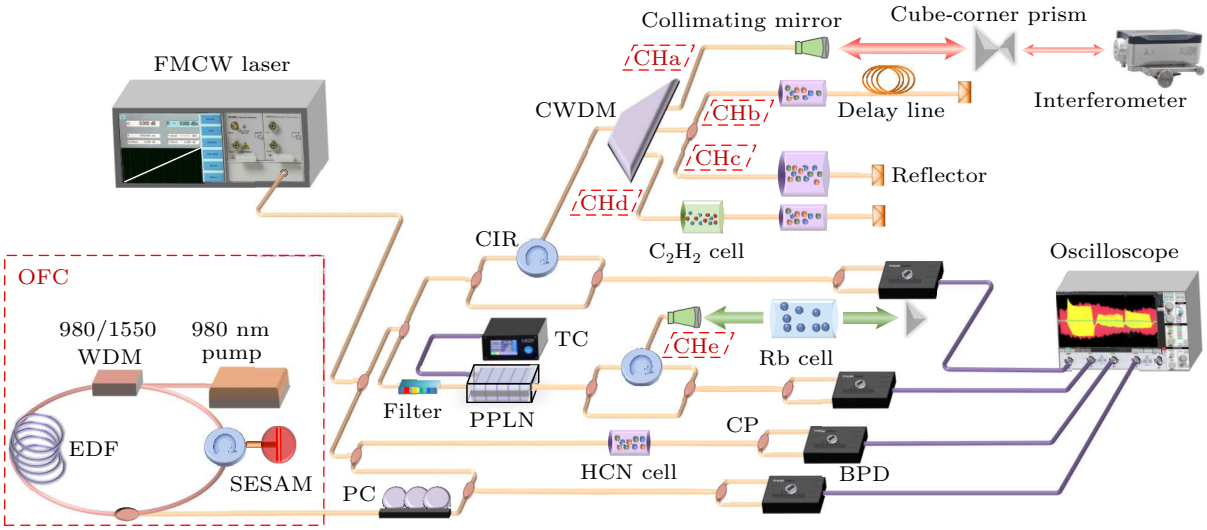


Fig. 3. Experimental system diagram. PC, polarization controller. EDF, erbium-doped fiber. SESAM, semiconductor saturable absorber mirror. BPD, balanced photodetector. TC, temperature controller.

4. Experiments and discussion

4.1. Nonlinear calibration and high precision optical path measurement

Sections of the original time domain waveforms corresponding to the 5 channels, namely, CHa–Che are shown in Figs. 4(a)–4(d). Figure 4(e) shows sections of the time-domain waveforms corresponding to the frequency marking and calibration paths, including the extraction of calibration points and the fitting results of the absorption peaks of the frequency marking paths. Figure 4(f) shows the spectral diagram of OFC, whose bandwidth can fully cover the scan frequency range of 1525 nm–1575 nm, meeting the requirement of frequency calibration. Since the tunable laser scans the frequency range of 1525 nm–1575 nm at the rate of 100 nm/s, and the repetition frequency of OFC is 200.15 MHz. Therefore, the calibration peak of the auxiliary interference optical path appears at a frequency of approximately 62.36 kHz. Approximately 31180 calibration peaks will be used for f_{FM}–φ_{M} fitting during a 50 nm scan cycle, enabling the frequency nonlinear calibration.

Accurate extraction of calibration points is the key to ensuring the measurement accuracy. Here, the interference beat signal of the calibration path is self-convolved.[37] The process of convolution is the process of multiplying the interference signal and its corresponding points and summing the product, which can also be regarded as the result of weighted summing, which can achieve noise suppression and feature

enhancement in signal processing. The position point corresponding to the maximum value of the self-convolved value is then extracted, which is the equifrequency interval calibration point $f_{\mathrm{A}} = 0$. The frequency standard path is the direct absorbed signal of HCN, which is removed by SG filtering. Gaussian fitting is subsequently performed to obtain the absorption spectral line. The position of the extracted absorption peak value corresponds to the standard absorption wavelength provided by NIST standard reference data.

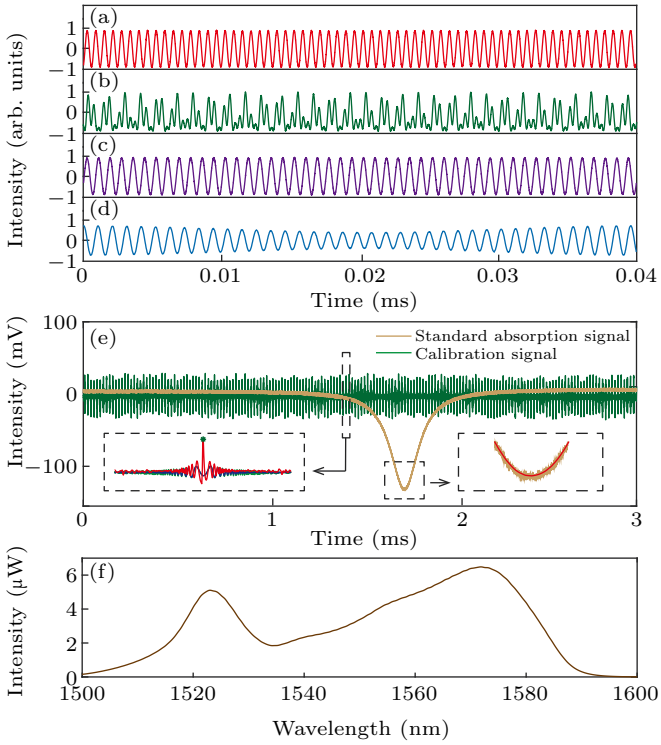


Fig. 4. Time domain waveforms of (a) CHa, (b) CHb and CHc, (c) CHd, (d) CHe, and (e) the frequency marking and calibration paths. (f) OFC spectrogram.

Combining the phase of the measurement path, the calibration points of the auxiliary path and the standard optical frequency information of the frequency standard path, the f_{FM}–φ_{M} line can be fitted by using the least-squares method, and the result is shown in Fig. 5(a). The residual difference between the fitted line and the original curve reflecting the tuning nonlinearity of the light source is also shown in Fig. 5(a). According to different f_{FM}–φ_{M} lines, the time domain signal can be interpolated and fitted according to the method described in Fig. 2, and the pseudo-frequency domain signal with a single frequency can be obtained.

DFT is performed on the obtained single-frequency sinusoidal signal to obtain the single-peak distance spectrum, as shown in Fig. 5(b). Different peak points correspond to different reflection peak positions, that is, the optical path to be measured. Figure 5(b) also shows the DFT results before nonlinear calibration. It can be seen that with the increase of the distance to be measured, the broadening of the range spectrum caused by nonlinearity becomes more and more serious. After nonlinear calibration, the single-peak signal is presented, which effectively inhibits the spectrum broadening and eliminates the nonlinear effect. In order to ascertain the high precision optical path measurement ability of the system, the cube-corner prism in CHa path is moved and the optical path measurement experiment of 6 position points is carried out in the path range of 20 m. The measurements are repeated 10 times at each position, while the oscilloscope data and the laser interferometer indication for calibration are recorded. The calculated optical path takes the standard value of $c = 299792458$ m/s. The calculated result is the absolute optical path. The experiment is carried out in a super-clean laboratory with constant temperature and humidity. The laser interferometer has temperature, humidity, and pressure measurement functions. Therefore, the environmental parameters can be measured in real time. Then, the numerical calibration between the optical path and the distance can be carried out according to the Edlen formula. Therefore, the result can be used as the standard of optical path measurement. Figure 5(c) shows the reflection peaks corresponding to 6 different positions, and the corresponding range-measuring error bar curves are shown in Fig. 5(d). According to the formula $\Delta L = c/(2B)$, the corresponding theoretical optical path measurement resolution is approximately 120 μm. Since the FMCW laser source is modulated by triangular waves, a single modulation cycle comprises two linear frequency modulation processes. Furthermore, the final result is the average of the measured data over 10 modulation cycles. It can be seen from the experimental results that the standard deviation of the optical path measurement is less than 10 μm,

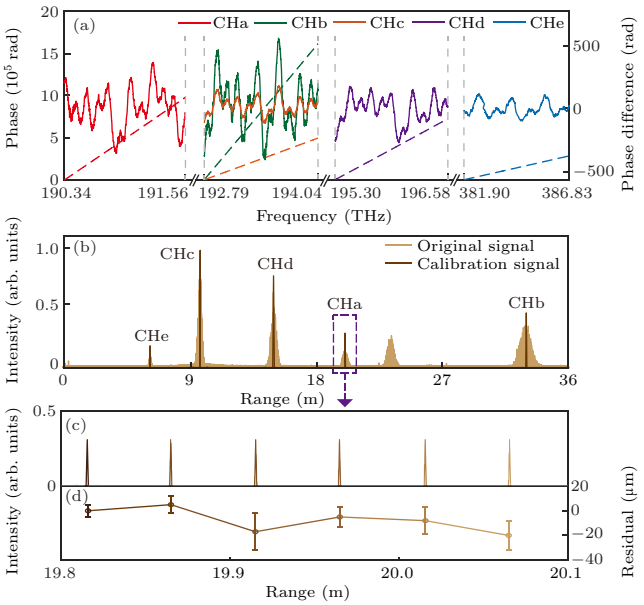


Fig. 5. (a) The f_{FM}–φ_{M} fitting curves and fit residuals. The dashed line represents the straight line fits, corresponding to the left ordinate. The solid line is the fitting residual, corresponding to the right ordinate. (b) Reflection peaks before and after nonlinear calibration for the 5-channel parallel measurement. (c) Reflection peaks at different locations of CHa. (d) Error bar diagram of optical path measurement results.

and the maximum displacement error of the average value of 10 measurements at each point is less than 20 μm compared with the standard value. These results establish that micron level measurement accuracy is realized, thereby verifying the positioning capability of the system for the measured target point.

4.2. Multiplexed molecular absorption spectrum measurement

The absorption spectrum information is retrieved by IFT for obtaining distance spectrum data. 5000 points near the reflection peak of the five signals are symmetrically intercepted for IFT calculation, and the mode square is taken to obtain the transmitted signal. The absorption line with normalization and interpolation fitting is shown in Fig. 6. Among them, CHb and CHc contain HCN cells of different densities, CHd contains both HCN and C_2H_2 cells, and CHe contains an Rb cell, thus showing corresponding absorption spectral lines.

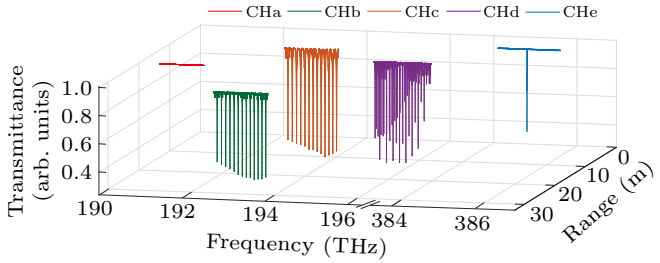


Fig. 6. Inversion results of multiplexed absorption spectra.

Firstly, the measurement accuracy of molecular absorption spectrum is analyzed. Figures 7(a) and 7(b) show the absorption spectrum waveform and the error bar curve of the absorption peak frequency measurement of the CHd channel, respectively. The wavelength ranges of R11–R25 containing HCN and P16–P1 containing C_2H_2 are selected for analysis. According to the formula $\Delta f = B/M$, the frequency resolution is 250 MHz. The mean and standard deviation of 10 repeated measurements are calculated and their values are compared with the values given by NIST standard reference data to obtain the error bar curve. The results show that the indication error of the absorption peak frequency measurement is less than 150 MHz, which proves that the system can realize the pm-level high precision gas absorption spectrum detection and accurately distinguish the different components in the gas mixture.

Figure 8 shows the measurement results of 13 absorption lines of P16–P4 of HCN for CHb and CHc. Figure 8(a) shows the measured absorption lines. Figure 8(b) shows the error bar curve of the absorption peak frequency measurement. It can be seen that the indicated error of the absorption peak frequency measurement is within 150 MHz. To further analyze the inversion accuracy of absorption lines, a spectrometer (Yokogawa AQ6370D) is used to record the spectral information of OFC before and after passing through different HCN chambers. The normalized result of the absorption spectral line can be used as a reference standard value for measurement, as shown in Fig. 8(d). Figure 8(c) shows that the residual difference between the measured spectral line and the reference spectral line is within 0.04. This result verifies the ability of the system to accurately obtain the gas absorption spectrum information in the multiplexed measurement scenario.

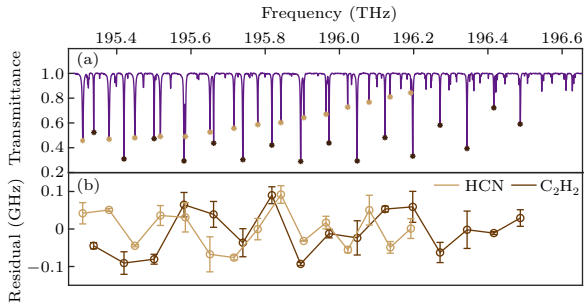


Fig. 7. Absorption spectrum inversion results of CHd. (a) Absorption lines of HCN and C_2H_2. (b) Measurement error of HCN and C_2H_2 absorption peak frequency.

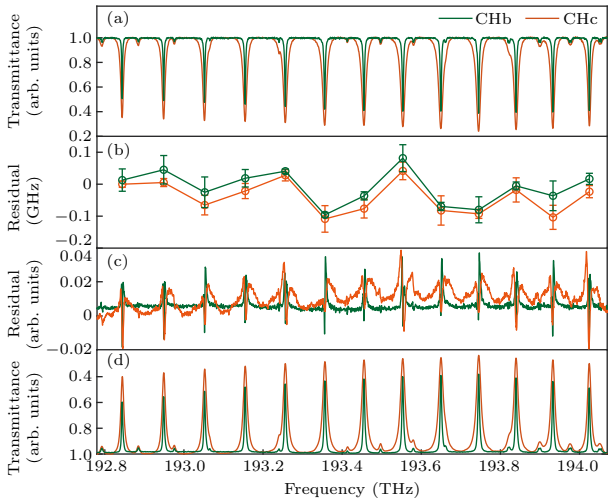


Fig. 8. Absorption spectrum inversion results of CHb and CHc. (a) Absorption lines of HCN. (b) Absorption peak frequency measurement error. (c) Residual of absorption line inversion. (d) Standard absorption lines.

4.3. Laser frequency doubling atomic absorption spectrum measurement

The Rb gas cell used in the experiment contains 72.15% ^{85}Rb and 27.85% ^{87}Rb with natural isotope ratio, and its hyperfine structure is shown in Fig. 9.[38] Figure 10(a) shows the absorption spectra of Rb obtained by experiment. Since the incident and reflected light power through the Rb cell is less than 100 μW and the power of the two beams of light is close, the saturation absorption effect is not considered. The wavelength of the laser after frequency doubling is near 780 nm, and the corresponding frequency is 384.615 THz.

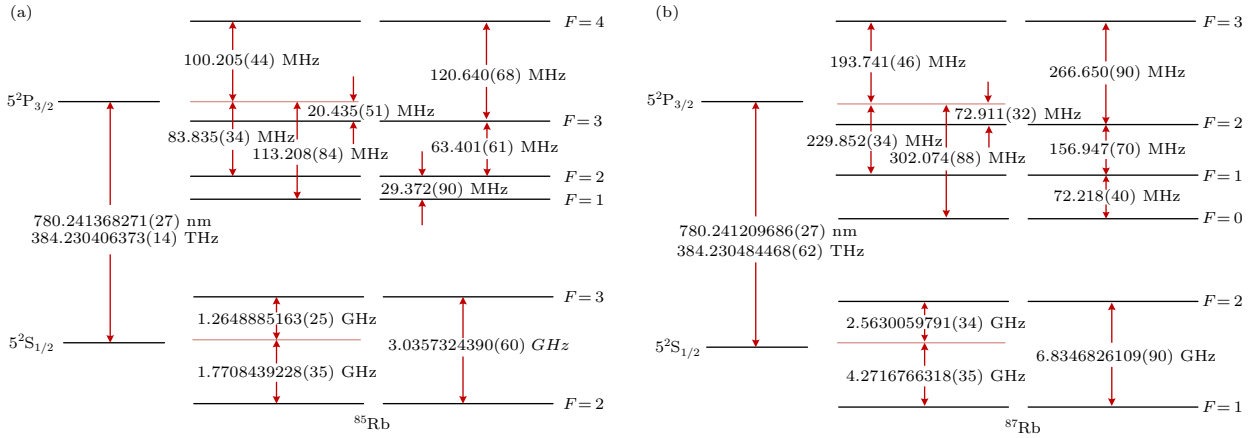


Fig. 9. Energy level diagrams of (a) ^{85}Rb and (b) ^{87}Rb.

Therefore, only the $5^2S_{1/2} \rightarrow 5^2P_{3/2}$ transitions between ^{85}Rb and ^{87}Rb need to be considered. According to data in Fig. 9 and Table 1, accounting for the Doppler broadening of the absorption spectrum, the corresponding transition frequencies of ground state ^{87}Rb($F=2$), ^{85}Rb($F=3$), ^{85}Rb($F=2$) and ^{87}Rb($F=1$) are about 384.228 THz, 384.229 THz, 384.232 THz and 384.235 THz, respectively, which are consistent with the obtained absorption peak frequencies. And the standard deviation of 10 repeated measurements is less than 50 MHz. Since the theoretical transition frequencies and the measured values coincide well, the feasibility of FMCW frequency doubling detection for realizing precise spectral line resolution and sample component identification of atomic gas chamber is verified.

Table 1. Intrinsic saturation absorption frequency of ^{85}Rb and (b) ^{87}Rb.

	Ground state	Excited state	Spectral frequency (THz)
^{85}Rb	$F=2$	$F=3$	384.232157
		$F=2$	384.232093
		$F=1$	384.232064
	$F=3$	$F=4$	384.229242
		$F=3$	384.229121
		$F=2$	384.229058
^{87}Rb	$F=1$	$F=2$	384.234683
		$F=1$	384.234526
		$F=0$	384.234545
	$F=2$	$F=3$	384.228115
		$F=2$	384.227849
		$F=1$	384.227692

In addition, FMCW has the advantage of real-time online measurement. For this study, a positive temperature coefficient (PTC) heating sheet is used to rapidly increase the temperature of the steam cell from room temperature (25 °C) to 40 °C in 30 s, with a time resolution of 0.65 s. As shown in Fig. 10(c), the absorbed signal strength, Rb, gradually increases, and spectral lines gradually widen with an increase in temperature. The main reason is that the total atomic number density in the gas chamber shows an exponential growth trend with an increase in temperature. However, the calculated absorption peak frequency remains unchanged, which further verifies the real-time dynamic measurement capability of the system.

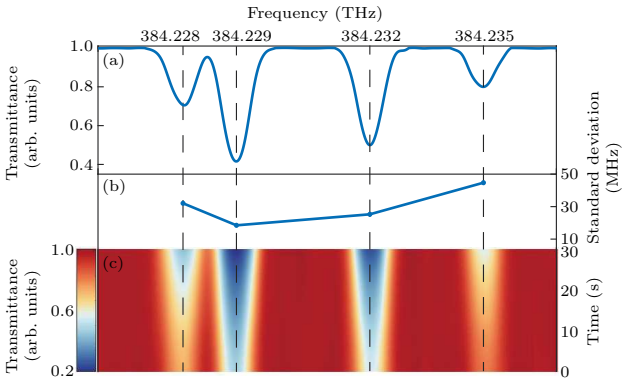


Fig. 10. Absorption spectrum inversion results of Rb. (a) Rb absorption line. (b) The standard deviation of Rb broadening absorption peak frequency measurement. (c) Results corresponding to measurements involving a rapid temperature increase.

5. Conclusion

In summary, a FMCW multiplexed absorption spectrum sensing device based on OFC calibration tuning nonlinearity is implemented for precisely and synchronously measuring the absorption spectrum and the multiplexed optical path for multiple target points. Combined with the WDM characteristics of the wide spectrum FMCW light source and the FDM characteristics of the coherent detection signal, the number of parallel measurement channels is greatly expanded. Furthermore, when combined with a PPLN frequency multiplier crystal, the absorption spectrum can be detected across hundreds of nanometers, which enables the simultaneous absorption spectrum measurement of molecular and atomic samples. A stable and broad-spectrum OFC is used as the calibration source for tuning nonlinearity, and high-precision nonlinear calibration is realized. A single calibration signal can be used for frequency calibration of all multiplexed channel signals at the

same time. Firstly, the effect of frequency jitter of the light source is removed by nonlinear calibration. Secondly, the optical path value is obtained by DFT, and the multi-channel signal is distinguished. Finally, the IFT operation is performed on the DFT signal to inverse the absorption spectrum. This enables the multi-parameter measurements. The experimental results from a 5-channel measurement system show that the measurement accuracy of the absorption peak wavelength is better than 150 MHz, and the optical path measurement accuracy can reach 20 μm. The system can realize the accurate inversion of several types of absorption lines with different densities. Furthermore, the identification of different gases can be achieved in multi-gas component scenarios in continuous, real-time and online measurement configurations. The system is capable of wide spectrum, multi-component, high precision, multiplexed and multi-parameter measurement. Additionally, it has a large dynamic range and can support non-contact measurements, which demonstrates strong adaptability to harsh environments. The proposed gas sensing device demonstrates practical value in the field of gas absorption spectrum detection and related instrument industry, and has application potential in military, industrial and research applications.

Appendix A: Principle of frequency-modulated nonlinearity calibration

Figure 1 shows the schematic diagram of the optical path of FMCW absorption spectrum measurement. FMCW laser emits a triangular-wave FM laser whose frequency changes in a periodic triangle; it increases and then periodically decreases. Only the previous half cycle is used as an example here. After splitting the beam, the outgoing laser enters the MZI measurement path and the tuned nonlinear calibration path based on OFC. In the measurement path, the FM laser is divided into beams again. A beam returns from the original path after passing through the path to be measured. As an echo signal, the beam is combined with the other vibrating light through the coupler, and the optical path difference is $2L$.

Let the modulation bandwidth be B and the period be t_{T}. Ideally, the change of the outgoing laser frequency with time t can be expressed as follows:

$$f_{\mathrm{FM}}(t) = f_0 + \alpha t, \tag{A1}$$

where f_0 is the initial frequency, and $\alpha = 2B/t_{\mathrm{T}}$ is the modulation rate.

The instantaneous phase $\varphi_{\mathrm{M}}(t)$ can be expressed as follows:

$$\begin{aligned}\varphi_{\mathrm{M}}(t) &= 2\pi \cdot \int_0^t f_{\mathrm{FM}}(t)\,\mathrm{d}t + \varphi_0 \\ &= 2\pi \cdot t^2 \cdot \frac{\alpha}{2} + 2\pi \cdot f_0 \cdot t + \varphi_0,\end{aligned} \tag{A2}$$

where φ_0 is the initial phase.

Let the amplitude of the local oscillator light of the measurement path be i_0. Then, the laser electric field equation of the local oscillator light can be expressed as follows:

$$E_{\mathrm{LO}}(t) = i_0 \cdot \exp\left\{\mathrm{j}\left[2\pi \cdot t^2 \cdot \frac{\alpha}{2} + 2\pi \cdot f_0 \cdot t + \varphi_0\right]\right\}. \tag{A3}$$

Let the speed of light in a vacuum be c and the refractive index of the medium be n. Compared with the local oscillator light, the measured light passes through an optical path with a distance of L, resulting in a delay $\tau = 2Ln/c$. If the optical amplitude of the return wave is i, then the echo signal can be expressed as follows:

$$\begin{aligned}&E_{\mathrm{SI}}(t,\tau) \\ &= i \cdot \exp\left\{\mathrm{j}\left[2\pi \cdot (t+\tau)^2 \cdot \frac{\alpha}{2} + 2\pi \cdot f_0 \cdot (t+\tau) + \varphi_0\right]\right\}.\end{aligned} \tag{A4}$$

Local vibration and echo signals interfere in the coupler, and photoelectric conversion is carried out by a photoelectric detector. If E_{LO}^* and E_{SI}^* are the conjugate expressions of the local oscillator light and the measured photoelectric field, the light intensity of the interference signal changes as follows:

$$\begin{aligned}I(t,\tau) &= (E_{\mathrm{LO}} + E_{\mathrm{SI}}) \cdot (E_{\mathrm{LO}}^* + E_{\mathrm{SI}}^*) \\ &= |E_{\mathrm{LO}}|^2 + |E_{\mathrm{SI}}|^2 + 2(E_{\mathrm{LO}} \cdot E_{\mathrm{SI}}) \\ &\quad \times \cos\left[2\pi \cdot \left(\frac{\alpha}{2}\tau^2 + f_0 \cdot \tau + \alpha \cdot \tau \cdot t\right)\right].\end{aligned} \tag{A5}$$

When the signal is collected, the direct current (DC) component is filtered out and simplified to

$$I(t,\tau) = V \cdot \sqrt{i_0 \cdot i} \cdot \cos\left[2\pi \cdot \left(\frac{\alpha}{2}\tau^2 + f_0 \cdot \tau + \alpha \cdot \tau \cdot t\right)\right], \tag{A6}$$

where V is a constant coefficient. Since τ is usually less than 10^{-5}, and α and f_0 are more than 10^{13}, $\alpha\tau^2/2$ is much smaller than the other two terms inside the cosine function; hence, it can be neglected,

$$I(t,\tau) = V \cdot \sqrt{i_0 \cdot i} \cdot \cos\left[2\pi \cdot (f_0 \cdot \tau + \alpha \cdot \tau \cdot t)\right]. \tag{A7}$$

Therefore, under ideal conditions, the standard cosine signal with frequency $f_{\mathrm{M}} = \alpha\tau$ can be acquired by the data acquisition system.

The actual laser output is not an ideal triangular modulated signal. Let $f_{\mathrm{e}}(t)$ be the modulation nonlinear term, then the outgoing light frequency can be expressed as

$$f_{\mathrm{FM}}(t) = f_0 + \alpha \cdot t + f_{\mathrm{e}}(t). \tag{A8}$$

The local oscillator light entering the coupler and the measured photofield equations are expressed as

$$\begin{aligned}E_{\mathrm{MLO}}(t) &= i_0 \cdot \exp\left\{\mathrm{j}\left[2\pi \cdot t^2 \cdot \frac{\alpha}{2} + 2\pi \cdot f_0 \cdot t\right.\right. \\ &\quad \left.\left. + \varphi_0 + 2\pi \cdot \int_0^t f_{\mathrm{e}}(t)\,\mathrm{d}t\right]\right\},\end{aligned} \tag{A9}$$

$$E_{\mathrm{MSI}}(t,\tau) = i\cdot\exp\left\{\mathrm{j}\left[2\pi\cdot(t+\tau)^2\cdot\frac{\alpha}{2}+2\pi\cdot f_0\cdot(t+\tau)+\varphi_0+2\pi\cdot\int_0^{t+\tau} f_{\mathrm{e}}(t)\,\mathrm{d}t\right]\right\}. \tag{A10}$$

According to Eq. (A7), the change in the interference signal light intensity of the filtered DC component is

$$I(t,\tau) = V\cdot\sqrt{i_0\cdot i}\cdot\cos\left[2\pi\cdot\left(f_0\cdot\tau+\alpha\cdot\tau\cdot t+\int_t^{t+\tau} f_{\mathrm{e}}(t)\,\mathrm{d}t\right)\right]. \tag{A11}$$

Its instantaneous frequency is

$$f_{\mathrm{M}}(t) = \alpha\tau + f_{\mathrm{e}}(t). \tag{A12}$$

According to Eq. (A8), equation (A11) can be reduced to

$$I(t,\tau) = V\cdot\sqrt{i_0\cdot i}\cdot\cos\left[2\pi\cdot\int_t^{t+\tau} f_{\mathrm{FM}}(t)\,\mathrm{d}t\right]. \tag{A13}$$

Fourier series expansion of the inner terms of the cosine function with respect to t can be expressed as follows:

$$2\pi\int_t^{t+\tau} f_{\mathrm{FM}}(t)\,\mathrm{d}t = 2\pi f_{\mathrm{FM}}(t)\cdot\tau + 2\pi\sum_{m=2}^{+\infty}\frac{\tau^2}{m!}\cdot f_{\mathrm{FM}}^{m-1}(t). \tag{A14}$$

Let $V_{\mathrm{M}} = V\cdot\sqrt{i_0\cdot i}$, ignore the higher order of τ, and substitute Eq. (A13):

$$I(t,\tau) = V_{\mathrm{M}}(t)\cdot\cos\left[2\pi\cdot f_{\mathrm{FM}}(t)\cdot\tau\right]. \tag{A15}$$

According to Eq. (A15), the phase of the ranging signal φ_{M} can be expressed as

$$\varphi_{\mathrm{M}}(t,\tau) = 2\pi\cdot f_{\mathrm{FM}}(t)\cdot\tau = \frac{4\pi\cdot L\cdot n}{c} f_{\mathrm{FM}}(t). \tag{A16}$$

When the distance L to be measured remains constant, φ_{M} and f_{FM} are primary functions of each other connected by $k = 4\pi\cdot L\cdot n/c = 2\pi\tau$. Then

$$\varphi_{\mathrm{M}}(t) = k\cdot f_{\mathrm{FM}}(t). \tag{A17}$$

For each change of fixed frequency Δf, the phase change of the measurement path is $\Delta\varphi_{\mathrm{M}} = k\cdot\Delta f$. Therefore, if Δf is known and the corresponding time of each equifrequency interval point can be extracted, the k value can be solved by calculating the corresponding φ_{M} value and using the least-square method to fit the straight line through the origin of f_{FM}–φ_{M}. Here, for the convenience of expression, equation (A17) is simplified to $\varphi = k\cdot f$, and R sets of single measurement data (f_p,φ_p) are used for line fitting. In the application of the least-square method, the quadratic residual sum of the measured value φ is required to be the smallest: $\sum_{p=1}^{R} v_p^2 = \sum_{p=1}^{R}(\varphi_p - k\cdot f_p)^2$. Therefore, the derivative of this equation with respect to k is 0. From this solution,

$$k = \frac{\sum_{p=1}^{R}\varphi_p\cdot f_p}{\sum_{p=1}^{R} f_p^2}. \tag{A18}$$

Therefore, in the case of instantaneous φ_{M} and f_{FM} measurement, the first function of f_{FM}–φ_{M} can be fitted by the least square method to solve the k value. Parameter φ_{M} can be solved directly by Hilbert transform, and f_{FM} can be calibrated by OFC.

The phase information can be obtained by using the Hilbert transform to calculate the phase $\varphi_{\mathrm{M}}(t)$ of the measuring circuit signal after achieving a $\pi/2$ phase shift. The Hilbert transformation of $I_{\mathrm{M}}(t)$ is equivalent to convolving it with $1/(\pi t)$, obtaining the time-domain expression

$$h_{\mathrm{M}}(t) = I_{\mathrm{M}}(t)\otimes\frac{1}{\pi t} = \frac{1}{\pi}\int_{-\infty}^{+\infty}\frac{I_{\mathrm{M}}(\tau)}{t-\tau}\,\mathrm{d}\tau. \tag{A19}$$

Parameters $I_{\mathrm{M}}(t)$ and $h_{\mathrm{M}}(t)$ form conjugate complex numbers for Cauchy principal value integrals. Hence, a new analytic signal $H_{\mathrm{M}}(t)$ can be obtained as

$$H_{\mathrm{M}}(t) = I_{\mathrm{M}}(t) + j\cdot h_{\mathrm{M}}(t) = \sqrt{I_{\mathrm{M}}^2(t)+h_{\mathrm{M}}^2(t)}\cdot\exp\left[\mathrm{j}\cdot\varphi_{\mathrm{M}}(t)\right]. \tag{A20}$$

Therefore, the phase of the measuring signal $\varphi_{\mathrm{M}}(t)$ can be solved by the inverse tangent transform

$$\varphi_{\mathrm{M}}(t) = \arctan\left[\frac{h_{\mathrm{M}}(t)}{I_{\mathrm{M}}(t)}\right]. \tag{A21}$$

The truncated phase value of $-\pi\sim\pi$ is obtained, and the continuous phase can be calculated after unwrapping.

The auxiliary path shown in Fig. 1 is used to obtain an equally spaced f_{FM} signal. The time domain pulse expression of the optical comb is

$$E_{\mathrm{comb}}(\omega) = i_{\mathrm{comb}}(t)\exp\left[\mathrm{j}\left(\omega_{\mathrm{c}}t+\varphi_{\mathrm{o}}+m\varphi_{\mathrm{ceo}}\right)\right]\otimes\sum_{m=-\infty}^{+\infty}\delta(t-mT_{\mathrm{r}}), \tag{A22}$$

where i_{comb} is the pulse envelope amplitude, ω_{c}, φ_{o}, and φ_{ceo} are the carrier frequency, initial phase, and carrier envelope phase shift, respectively, T_{r} is the pulse interval, and m is any integer. The phase difference between each pulse φ_{ceo} is constant.

Calculate the Fourier transform of Eq. (A22)

$$E_{\mathrm{comb}}(\omega) = i_{\mathrm{comb}}(\omega-\omega_{\mathrm{c}})\cdot\exp(\mathrm{j}\varphi_{\mathrm{o}})\times\sum_{m=-\infty}^{+\infty}\delta\left[\omega-2\pi(mf_{\mathrm{r}}+f_{\mathrm{ceo}})\right], \tag{A23}$$

where $f_r = 1/T_r$, equal to the reciprocal of the pulse period, is called the repetition frequency of the optical comb, generally MHz to GHz; $f_{ceo} = f_r \cdot \varphi_{ceo}/(2\pi)$ is the offset frequency caused by the carrier phase shift. The optical comb appears as a series of discrete broadband comb spectra with equal longitudinal mode interval f_r and initial frequency f_{ceo} in the frequency domain. The frequency corresponding to the N-th comb mode is $f_N = f_{ceo} + N \cdot f_r$.

The instantaneous frequency of the FMCW laser is f_{FM}, and the comb mark closest to its frequency is the Nth mode. Then

$$f_{FM} = f_N \pm f_A = f_{ceo} + N \cdot f_r \pm f_A, \tag{A24}$$

where f_A is the frequency of the interference beat signal generated by the laser to be measured, and the N-th comb mode, which can be measured by a photodetector.

For continuous-wave lasers with linear frequency modulation, f_{FM} is continuously tuned between comb modes with equal frequency distribution. The interference signal generated by the auxiliary calibration part is the triangular wave frequency modulation signal that changes continuously between 0 and $f_r/2$. Since f_r is usually several hundred MHz to several GHz, it is equivalent to low-pass filtering of the signal if the passband frequency of the photodetector is lower than 50 MHz in the auxiliary calibration part. Signal waveform information can only be observed on the oscilloscope alternating current (AC) when the frequency is close to 0, forming a calibration peak signal with an equal frequency interval f_r. The calibration point of equal frequency interval at $f_A = 0$ can be extracted by filtering and peak-seeking calculation.

The nonlinear calibration can be carried out under the condition that the intervals of φ_M and f_{FM} are calculated. The schematic diagram of the principle of nonlinear calibration is shown in Fig. 1(b), where the second quadrant represents the original time domain signal of the double optical path. The third quadrant contains the calibration point of equal frequency interval and corresponding φ_M. The fourth quadrant contains the f_{FM}–φ_M line obtained by fitting. After nonlinear calibration, φ_M is theoretically a linear function. Therefore, the single frequency sinusoidal signal shown in the first quadrant can be obtained by re-interpolating the measurement path signal. Since f_{FM} changes linearly with time after correction, the original time domain signal is transformed into the pseudo-frequency domain here, and the original time variable t is represented by the optical frequency variable f in the first quadrant of Fig. 1(b). Equation (A13) can be converted to

$$I(f,\tau) = V \cdot \sqrt{i_0 i} \cdot \cos(2\pi\tau f). \tag{A25}$$

On this basis, DFT calculation is carried out to obtain the pseudo-time domain signal shown in Fig. 1(c), whose peak position corresponds to the delay τ to be measured. The M data points are intercepted symmetrically on the left and right sides of the reflection peak, and the window function filtering is performed. IFT is applied to the filtered data to restore the timing information, and the absorption spectral curve in the optical frequency domain is obtained,[21,29] as shown in Fig. 1(d). The resolution of DFT is directly related to the sweep frequency range B of FMCW and can be expressed as $\Delta\tau = 1/B$. Therefore, the optical path measurement resolution is $L = c\tau/2$. The resolution of IFT also depends on the number of points M involved in the calculation, which can be expressed as $\Delta f = B/M$, that is, the spectral measurement resolution.

Acknowledgments

Project supported by the National Natural Science Foundation of China (Grant No. 52375546) and the National Key Research and Development Program of China (Grant No. 2022YFF0705701).

References

[1] Herman D I, Weerasekara C, Hutcherson L C, Giorgetta F R, Cossel K C, Waxman E M, Colacion G M, Newbury N R, Welch S M, DePaola B D, Coddington I, Santos E A and Washburn B R 2021 *Sci. Adv.* **7** 9765
[2] Rieker G B, Giorgetta F R, Swann W C, Kofler J, Zolot A M, Sinclair L C, Baumann E, Cromer C, Petron G, Sweeney C, Tans P P, Coddington I and Newbury N R 2014 *Optica* **1** 290
[3] Farooq A, Alquaity A B S, Raza M, Nasir E F, Yao S C and Ren W 2022 *Prog. Energ. Combust.* **91** 100997
[4] Li A, Yao C H, Xia J F, Wang H J, Cheng Q X, Penty R, Fainman Y and Pan S L 2022 *Light-Sci. Appl.* **11** 174
[5] Zhao R, Zhou B, Zhang J Y, Cheng R X, Liu Q, Dai M L, Wang B B and Wang Y H 2023 *Exp. Therm. Fluid Sci.* **147** 110930
[6] Yang Z Y, Albrow-Owen T, Cai W W and Hasan T 2021 *Science* **371** eabe0722
[7] Yun D V, Cole R K, Malarich N A, Coburn S C, Hoghooghi N, Liu J W, France J J, Hagenmaier M A, Rice K M, Donbar J M and Rieker G B 2022 *Optica* **9** 15
[8] Coburn S, Alden C B, Wright R, Cossel K, Baumann E, Truong G W, Giorgetta F, Sweeney C, Newbury N R, Prasad K, Coddington I and Rieker G B 2018 *Optica* **5** 320
[9] Lu P, Lalam N, Badar M, Liu B, Chorpening B T, Buric M P and Ohodnicki P R 2019 *Appl. Phys. Rev.* **6** 041302
[10] Huang X L, Li N, Weng C S and Kang Y 2022 *Chin. Phys. B* **31** 014703
[11] Nie W, Xu Z Y, Kan R F, Dong M R and Lu J D 2021 *Chin. Phys. B* **30** 064213
[12] Wang Q J, Sun P S, Zhang Z R, Zhang L W, Yang X, Wu B, Pang T, Xia H and Li Q Y 2021 *Acta. Phys. Sin* **70** 144203 (in Chinese)
[13] Zhang W P, Chen X Y, Wu X J, Li Y and Wei H Y 2019 *Photonics Res.* **7** 883
[14] Peng D W, Gu C L, Zuo Z, Di Y F, Zou X, Tang L L, Deng L H, Luo D P, Liu Y and Li W X 2023 *Nat. Commun.* **14** 883
[15] Di Rosa M D, Reiten M T, Mertes K M and Clegg S M 2021 *Opt. Express* **29** 26456
[16] Yuan Z Y, Lou X T and Dong Y K 2021 *J. Lightwave Technol* **39** 4847
[17] Yuan Z Y, Lou X T, Chu Q, Li T F and Dong Y K 2022 *Appl. Phys. B* **128** 66
[18] Wang C, Langrock C, Marandi A, Jankowski M, Zhang M, Desiatov B, Fejer M M and Loncar M 2018 *Optica* **5** 1438
[19] Jankowski M, Langrock C, Desiatov B, Marandi A, Wang C, Zhang M, Phillips C R, Loncar M and Fejer M M 2020 *Optica* **7** 40
[20] Konishi T, Iiyama K and Yoshii Y 2021 *Opt. Commun.* **498** 127208

[21] Lou X T, Feng Y B, Chen C and Dong Y K 2020 *Opt. Express* **28** 9014
[22] Diddams S A, Vahala K and Udem T 2020 *Science* **369** eaay3676
[23] Hashimoto K, Nakamura T, Kageyama T, Badarla V R, Shimada H, Horisaki R and Ideguchi T 2023 *Light-Sci. Appl.* **12** 48
[24] Liu C H, Jin H S, Liu H and Bai J T 2022 *Chin. Phys. B* **31** 084205
[25] Cao S Y, Han Y, Ding Y J, Lin B K and Fang Z J 2022 *Chin. Phys. B* **31** 074207
[26] Zhang P, Zhang Y Y, Li M K, Rao B J, Yan L L, Chen F X, Zhang X F, Chen Q F, Jiang H F and Zhang S G 2022 *Chin. Phys. B* **31** 054210
[27] Scholkmann F, Kleiser S, Metz A J, Zimmermann R, Pavia J M, Wolf U and Wolf M 2014 *Neuroimage* **85** 6
[28] Jia L H, Wang Y, Wang X Y, Zhang F M, Wang W Q, Wang J D, Zheng J H, Chen J W, Song M Y, Ma X, Yuan M Y, Little B, Chu S T, Cheng D, Qu X H, Zhao W and Zhang W F 2021 *Opt. Lett.* **46** 1025
[29] Lou X T, Feng Y B, Yang S H and Dong Y K 2021 *Photonics Res.* **9** 193
[30] Zavrsnik M and Stewart G 2000 *J. Lightwave Technol.* **18** 57
[31] Jiang Y S, Karpf S and Jalali B 2020 *Nat. Photonics* **14** 14
[32] Riemensberger J, Lukashchuk A, Karpov M, Weng W L, Lucas E, Liu J Q and Kippenberg T J 2020 *Nature* **581** 164
[33] Liu Y, Xia W Z, He M Z, Cao S Y, Miao D J, Lin B K, Xie J D, Yang W L and Li J S 2022 *Opt. Laser Eng.* **151** 106900
[34] National Institute of Standards and Technology https://www.nist.gov/srd
[35] Li J S, Deng H, Li P F and Yu B L 2015 *Appl. Phys. B* **120** 207
[36] Jia L H, Jin B, Zheng J H, Zhang F M and Qu X H 2024 *J. Lightwave Technol.* **42** 1710
[37] Niu Q, Zheng J H, Cheng X R, Liu J C, Jia L H, Ni L M, Nian J, Zhang F M and Qu X H 2022 *Opt. Express* **30** 35029
[38] Steck D A 2023 *Rubidium 85 D Line Data* (revision 2.3.2) (Eugene: University of Oregon) pp. 25–27